Research Article

Zhonghui Wang, Qiang Gao, Haihang Luo, Haojun Fan*, Yi Chen, and Jun Xiang

In situ synthesis of reduced graphene oxide/$SnIn_4S_8$ nanocomposites with enhanced photocatalytic performance for pollutant degradation

https://doi.org/10.1515/ntrev-2024-0012
received November 29, 2023; accepted March 19, 2024

Abstract: A type of reduced graphene oxide (rGO)/$SnIn_4S_8$ (SIS) nanocomposites was successfully fabricated by a facile and efficient microwave-assisted method. Their morphology, structure, composition, and optical performance were investigated by different analytical techniques, respectively. The results indicated that rGO had an important effect on the structure of photocatalysts. As the content of rGO increases, the unchin-like microsphere structure of rGO/SIS evolved gradually into aggregated nanosheet structure. The photocatalytic degradation experiments were carried out under visible light irradiation. The results demonstrated rGO/SIS-2 nanocomposites exhibited higher photocatalytic activity toward the degradation of RhodamineB than that of SIS, rGO/SIS-1 as well as rGO/SIS-3. Meanwhile, the mineralization efficiency of Rhodamine B (RhB) can reach up to 73.8% within 30 min. Interestingly, rGO/SIS-2 nanocomposites exhibited excellent recycle stability with 96% removal efficiency of RhB after three cycles. The enhanced photocatalytic activity of rGO/SIS-2 nanocomposites should be attributed to the strong interaction of rGO and SIS, the decrease of band gap energy, the enhanced visible light absorption, and excellent electrons' mobility of rGO, thereby promoting charge separation. Finally, the mechanism of rGO/SIS nanocomposites for the degradation of RhB has been also proposed. This work provides a facile and efficient pathway to prepare SIS-based nanocomposites with enhanced catalytic efficiency by combining the advantages of microwave-assisted heating and incorporating carbon-based nanomaterials for the degradation of organic pollutants in visible light irradiation.

Keywords: visible light driven, nanocomposites, reduced graphene oxide/$SnIn_4S_8$, microwave-assisted, photocatalytic performance

1 Introduction

With the rapid development of the industrial economy and society, water pollution has become a global problem. Organic dyes, a type of significant pollutants, are widely applied in textile, paint and pigments, leather manufacturing, indicators, and so on [1]. For example, Rhodamine B (RhB) and methylene blue (MB) are widely used organic dyes in industry and laboratory and have been one of the dye pollutants. Water pollution caused by these dyes poses a potential threat to the aquatic environment and human health owing to their complex aromatic structures, difficult degradation, and high toxicity [2,3]. In the past years, a number of strategies [4,5] including physical, chemical, and biological treatments have been developed for dye removal from wastewater. However, these traditional methods have some drawbacks [6], such as high cost, low efficiency, and incomplete detoxifying contaminants. Therefore, it is important to explore a facile, highly effective, energy-efficient, and producing no secondary pollution strategy for dye removal.

Semiconductor-based photocatalytic technology has attracted widespread attention [7–9] because of converting directly solar energy into chemical energy, sustainability, eco-friendly, high efficiency, and simple operation procedures. So far, a variety of semiconductor-based nanomaterials, including metal oxides [10–14], metal sulfides [15–17], as well as metal-organic frameworks (MOFs) [18,19], was

* **Corresponding author: Haojun Fan**, The Key Laboratory of Leather Chemistry and Engineering of Ministry of Education, Sichuan University, Chengdu 610065, Sichuan, China; National Engineering Research Center of Clean Technology in Leather Industry, Sichuan University, Chengdu 610065, Sichuan, China, e-mail: fanhaojun@scu.edu.cn
Zhonghui Wang, **Qiang Gao**, **Haihang Luo**, **Yi Chen**, **Jun Xiang:** The Key Laboratory of Leather Chemistry and Engineering of Ministry of Education, Sichuan University, Chengdu 610065, Sichuan, China; National Engineering Research Center of Clean Technology in Leather Industry, Sichuan University, Chengdu 610065, Sichuan, China

widely reported for pollutant degradation. Among these photocatalysts, stannum indium sulfide ($SnIn_4S_8$, donated as SIS) with a suitable band gap (1.77–2.35 eV) and well relevant to the visible light absorption exhibits potential application in photocatalysis [20,21]. Unfortunately, for a single SIS semiconductor, the rapid electron–hole recombination will inhibit its photocatalytic efficiency [22]. Given this, a number of approaches have been explored to improve its photocatalytic activity, including metal doping [23], dye sensitization [24], incorporating of carbon-based nanomaterials [25,26], and coupling SIS with other nanomaterials [27]. For example, Sun *et al.* [28] fabricated tubular In_2O_3@$SnIn_4S_8$ hybrid photocatalysts by a two-step method and found that Cr(VI) reduction reaction constant *k* on these hybrid photocatalysts was 2.54 times higher than that of single $SnIn_4S_8$. Hu and coworkers [29] prepared $SnIn_4S_8$/BiOBr hybrid photocatalysts, which showed 99.8% of degradation efficiency (DE) for RhB within 40 min under visible light, while it was only 71.1% for single BiOBr.

Among nanomaterials, reduced graphene oxide (rGO) with the structure of a sp^2-bonded carbon atoms has attracted extensive attention owing to its exceptional properties such as large specific surface area, efficient visible light absorption, remarkable light transport, and superior electron mobility [30–32]. Generally, rGO as an excellent acceptor and mediator of photogenerated electrons was considered to be a perfect co-catalyst to improve the photocatalytic performance of semiconductors. Deng *et al.* [22] synthesized rGO/$SnIn_4S_8$ (SIS) composites *via* a low-temperature co-precipitation way for 5 h and discovered these composites could completely degrade RhB in 70 min. In our previous work [33], rGO/SIS photocatalysts assembled by hydrothermal method with 12 h exhibited an excellent reduction of Cr(VI). However, hydrothermal or low-temperature co-precipitation method for the preparation of rGO/SIS photcatalysts is time-consuming.

In recent years, the microwave-assisted method has drawn a lot of interest, by virtue of a lessened amount of reaction time from hours to minutes, uniform heat transfer, high yields, and high purity of the products [34–36]. For example, Song *et al.* [37] prepared Br/Bi_2WO_6 photocatalysts *via* microwave hydrothermal method with 2 h, and these photocatalysts exhibited 93% of DE for RhB in 120 min. They also prepared Br/Bi_2WO_6 photocatalysts *via* the hydrothermal method with a react time of 2 and 4 h, respectively. The results demonstrated that the DE of Br/Bi_2WO6 prepared by the microwave heating method was obviously higher than that of photocatalysts synthesized *via* the hydrothermal method. Thus, microwave-assisted method was considered to be an efficient and competitive method for preparing photocatalysts. Herein, we fabricated a type of rGO/SIS nanocomsposites with different amounts of rGO *via* microwave-assisted method. The introduction of rGO was designed to enhance the visible light absorption, decrease the band gap, and accelerate the separation and migration of photogenerated electrons-hole, and microwave irradiation was suggested to shorten the reaction time. Subsequently, the morphology and structure of rGO/SIS nanocomposites were investigated. The as-prepared nanocomposites were employed to degrade RhB and MB under visible light illumination. The results displayed rGO/SIS-2 photocatalysts showing significantly enhanced photocatalytic activity than that of rGO/SIS-1, rGO/SIS-3, and SIS. The recycle stability of rGO/SIS hybrid photocatalysts was also observed. Finally, a probable photocatalytic mechanism was proposed. This work provides a facile and efficient pathway to prepare SIS-based nanocomposites by combining the advantages of microwave-assisted heating and incorporating carbon-based nanomaterials for the degradation of organic pollutants in visible light irradiation with enhanced catalytic efficiency.

2 Experiment

2.1 Materials

Graphite oxide was observed from Kelong Chemical Incorporated Co., Ltd., China. Thioacetamide (TAA), tin chloride pentahydrate ($SnCl_4{\cdot}5H_2O$), cetyl-methyl-ammoniumbromide (CTAB), Rhodamine B, and indium chloride tetrahydrate ($InCl_3{\cdot}4H_2O$) were provided by Aladdin Ltd, China. All reagents were of analytical grade and used as received without any further purification.

2.2 Preparation of rGO/SIS nanocomposites

Graphene oxide (GO) was prepared following the Hummers' method with a slight modification [38]. For the fabrication of a series of rGO/SIS nanocomposites, a certain amount of GO was dispersed into 50 mL of ethyl alcohol by ultrasonication for 30 min. Then, 0.15 mmol $SnCl_4{\cdot}5H_2O$, 0.6 mmol $InCl_3{\cdot}4H_2O$, 20 mg CTAB, and 0.0902 g TAA were added into aforementioned GO solution and maintained vigorous stirring for 40 min. Subsequently, the above-mentioned solution was placed into a 100 mL Teflon tube of a microwave synthesis reactor with a stirring bar and a fiber optic sensor (Multiwave PRO, Anton Paar). The sealed vessel was treated at 160°C within 5 min of a ramping time and kept for 20 min. After reaction, the vessels were quickly cooled down to 55°C *via* the

default microwave system-cooling program. Then, the microwave-safe tube was taken out from the microwave reactor. Finally, the clay bank precipitates were separated by centrifugation, washed with water and absolute ethyl alcohol respectively, and freeze-dried for further use. The obtained nanocomposite was denoted as rGO/SIS-1 (rGO/SIS-0.5%, 0.5% is the initial weight ratio of GO and SIS, same below), rGO/SIS-2 (rGO/SIS-1%), and rGO/SIS-3 (rGO/SIS-2%). For comparison, SIS was also fabricated with the same microwave-assisted method without GO.

2.3 Characterization

Surface morphologies of a series of as-prepared rGO/SIS nanocomposites were visualized by a scanning electron microscopy (SEM) with the party of energy dispersive spectrometry (JSM7500F, Japan). X-ray photoelectron spectroscopy (XPS) was performed on an XPS system (AXIS Supra, Kratos) with an Al Ka. The crystalline structure of as-prepared rGO/SIS nanocomposites was recorded by a Philips X-ray diffraction (XRD) with Cu-Kα radiation. To evaluate the optical performance, UV–vis diffuse reflectance spectra (DRS) analysis of a series of as-prepared rGO/SIS nanocomposites was carried out on a PerkinElmer 1050 + UV–vis spectrometer using $BaSO_4$ as a reference. To explore the separation efficiency of photogenic charge carriers, photoluminescence (PL) spectra of a series of rGO/SIS nanocomposites were obtained by a fluorescence spectrometer with a photomultiplier voltage of 700 V and an excitation wavelength of 370 nm (F-7100, Hitachi, Japan). Fourier transform infrared spectroscopy (FT-IR) analysis of rGO/SIS nanocomposites was surveyed *via* a PerkinElmer spectrum 3 FT-IR spectrophotometer using KBr as the reference in a wavenumber range from 400 to 4,000 cm^{-1}. The total organic carbon (TOC) of rGO/SIS nanocomposites was monitored *via* a TOC cube analyser (elementar, vario TOC, Germany).

2.4 Photocatalytic experiments

The photocatalytic activities of SIS, rGO/SIS-1, rGO/SIS-2, and rGO/SIS-3 nanocomposites were studied by observing DE of RhB and MB. 10 mg of samples were added to 50 mL of solution with 20 mg/L of RhB solution. Then, the suspension was ceaselessly stirred at room temperature in the dark for 1 h. Subsequently, the above-mentioned suspension was illuminated by 300 W Xe lamp (CEL-HXF300, China Education Au-light company) with a visible light filter (λ > 400 nm) at a distance of 10 cm. During the irradiation, 4 mL of suspension was quickly collected at predetermined time intervals and filtered by the 0.45 μm filter membrane. The absorbance of residual RhB was measured at 554 nm. The DE was evaluated by the following equation [39]:

$$\mathrm{DE} = (A_0 - A_t)/A_0 \times 100\%,$$

where A_0 and A_t represent the initial absorbance and absorbance at defined time intervals (t), respectively.

3 Results and discussion

3.1 Morphology

SEM was employed to gain insights into the morphologies of rGO/SIS-1, rGO/SIS-2, rGO/SIS-3, and SIS photocatalysts prepared by the microwave-assisted method within 20 min. As shown in Figure 1a, SIS exhibits an urchin-like microsphere structure fabricated by the disordered nanosheets intercrossing with about 1–2 μm in diameter, which is consistent with our previous report [40]. When a small amount of rGO is added, rGO/SIS-1 shows large-scale urchin-like microsphere structure (Figure 1b), which is similar to that of SIS. As the content of rGO increases, rGO/SIS-2 photocatalyst exhibits the hybrid structures of microspheres and nanosheets in Figure 1c. However, continuing to increase the content of rGO, rGO/SIS-3 photocatalyst displays aggregated nanosheets strucure (Figure 1d). These results indicated that rGO had an important effect on the structure of resultant photocatalysts. As the amount of rGO increased, the unchin-like microsphere structure of rGO/SIS evolved gradually into aggregated nanosheet structure. The reason may be that the low amounts of rGO were conductive to the self-assembly of rGO/SIS into unchin-like microspheres. However, with the increase in the amounts of rGO, the products are more inclined to form two-dimensional stacked assemblyies, resulting in large nanosheet structures.

3.2 The composition and structure

Energy dispersive spectrometry (EDS) was used to characterize the element distribution of rGO/SIS-2 nanocomposites. As illustrated in Figure 2a, Sn, In, S, C, and O elements are found in rGO/SIS nanocomposites, indicating the formation of the rGO/SIS nanocomposites. Additionally, Figure 2b–d displays the corresponding colored mapping images of rGO/SIS-2, which demonstrates the homogeneous distribution of Sn, In, S, C, and O elements in the whole rGO/SIS-2 nanocomposites.

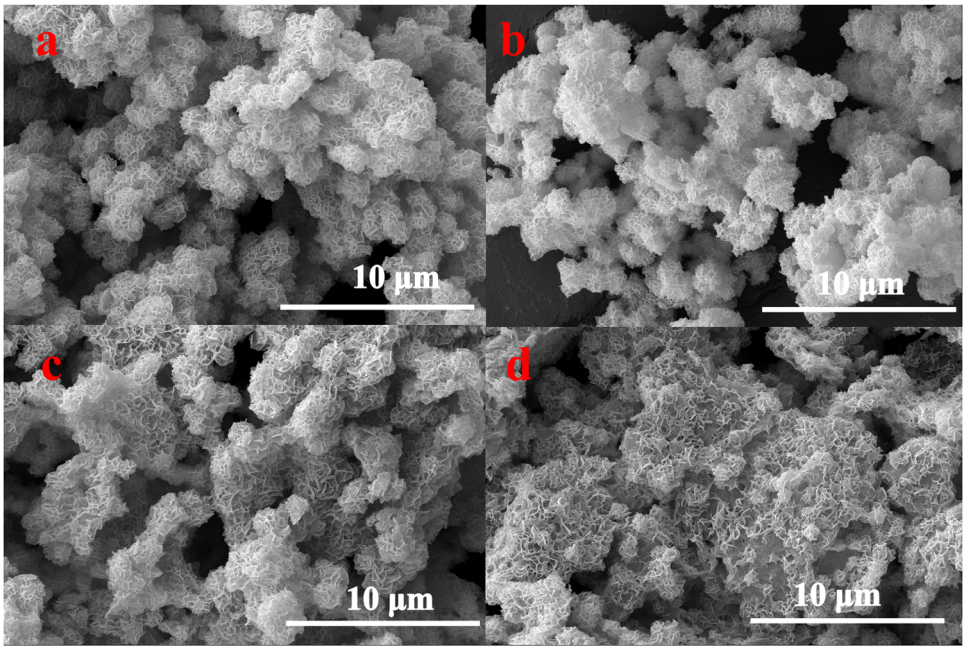

Figure 1: SEM images of (a) SIS, (b) rGO/SIS-1, (c) rGO/SIS-2, and (d) rGO/SIS-3.

XPS spectra were utilized to further investigate the composition and chemical valence state of rGO/SIS-2 nanocomposites. As predicted, the survey spectrum of rGO/SIS-2 photocatalysts identifies the existence of C, Sn, In, and S elements (Figure 3), which is consistent with the EDS results. In Figure 4a of C 1s high-resolution spectrum for

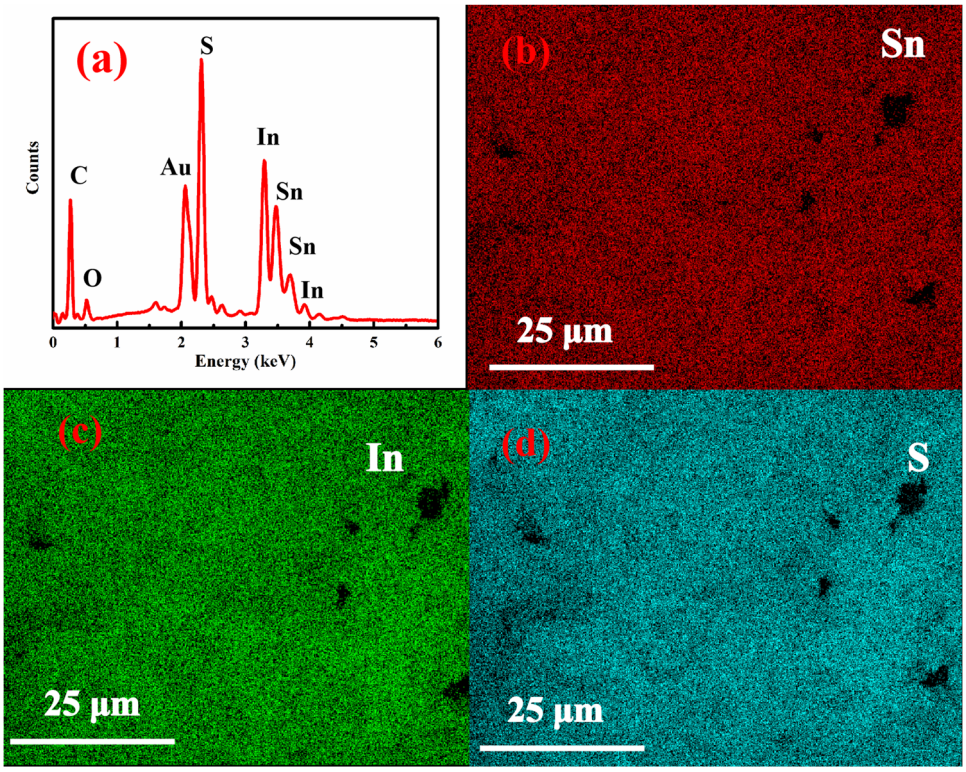

Figure 2: EDS spectrum (a) and (b–d) corresponding elemental mapping images of rGO/SIS-2.

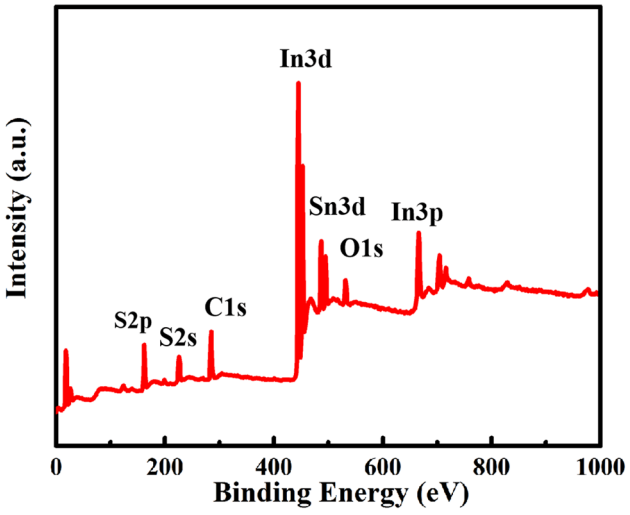

Figure 3: XPS survey of rGO/SIS-2 nanocomposites.

GO, three obvious peaks located at 285.1, 287.7, and 288.91 eV can be assigned to C═C, C═O, and O═C–O, respectively. For rGO/SIS-2 photocatalysts, the three characteristic binding energies of 284.8, 286.2, and 288.9 eV are less than that of GO. Meanwhile, the two peaks' intensity of C═O and O═C–O oxygen-containing groups distinctly decreases, indicating the abundant reduction of GO in the formation of a series of rGO/SIS nanocomposites. In Figure 4b of Sn 3d spectra, the 486.7 and 495.1 eV should be assigned to Sn^{4+} $3d_{5/2}$ and Sn^{4+} $3d_{3/2}$, respectively. In Figure 4c, two main peaks situated at 445.1 and 452.6 eV are fitted into In^{3+} $3d_{5/2}$ and In^{3+} $3d_{3/2}$, respectively. In the S 2p spectrum, the two characteristic peaks located at 161.6 and 162.9 eV can be attributed to S $2p_{1/2}$ and S $2p_{3/2}$, respectively. Interestingly, compared with pure SIS, it can be found the characteristic peaks of Sn 3d, In 3d, and S 2p of rGO/SIS photocatalysts slightly shift to the higher binding energy. In general, the enhancements of

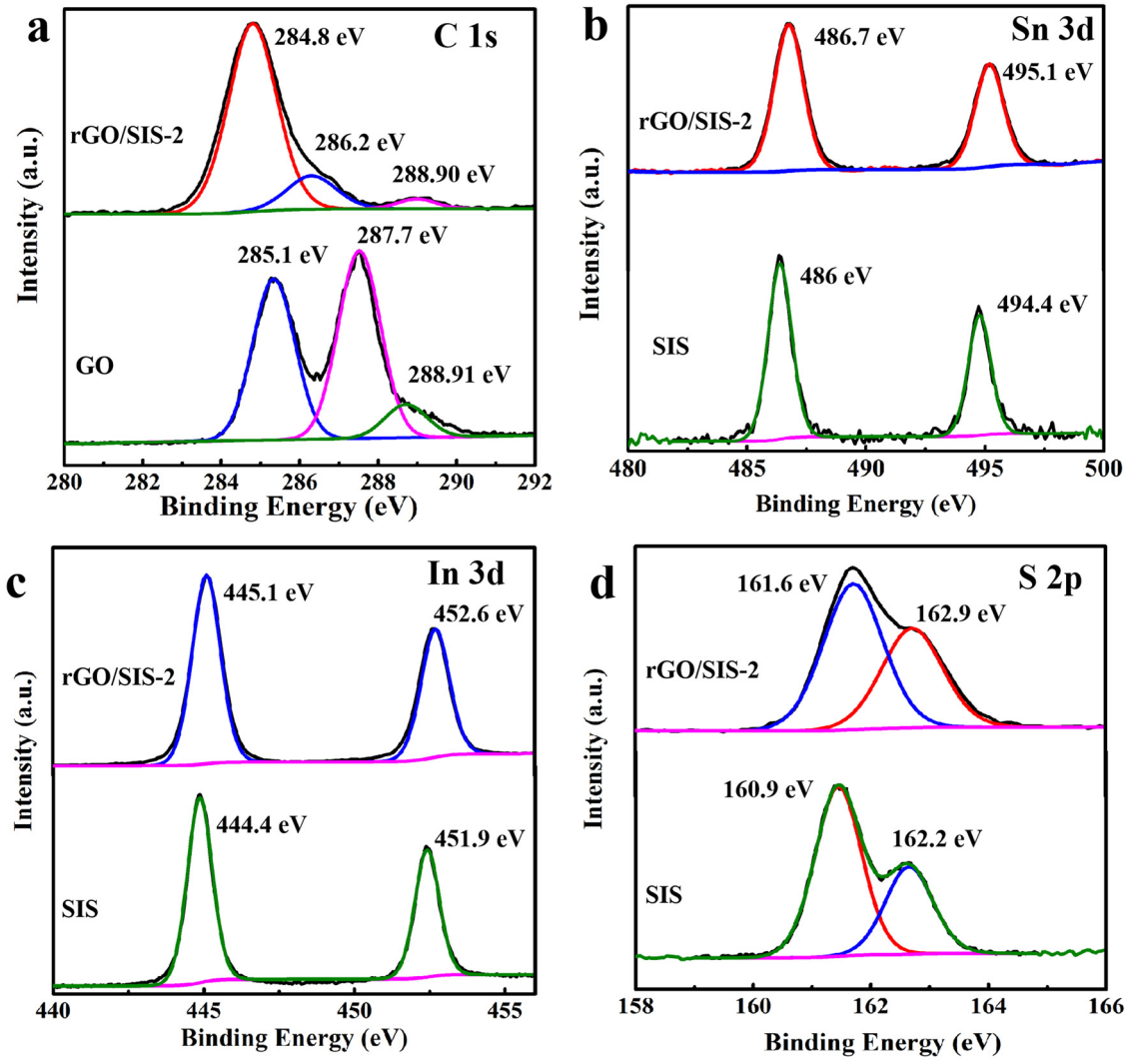

Figure 4: XPS spectra of rGO/SIS-2 and SIS: (a) C 1s, (b) Sn 3d, (c) In 3d, and (d) S 2p.

binding energy indicate the decrease of electron density, which results from the intense interaction of rGO and SIS. Therefore, the above results further proved the formation of rGO/SIS hybrid photocatalysts.

XRD patterns can be used to characterize the crystal structure of the SIS, rGO/SIS-1, rGO/SIS-2, and rGO/SIS-3 photocatalysts. As shown in Figure 5, the diffraction pattern of all samples prepared in the presence of different amounts of GO, concerning the number of peaks and assigned miller indices, is almost identical, confirming the successful preparation of rGO/SIS nanocomposites. It can be seen that six strong peaks located at 18.8, 27.3, 28.4, 33.2, 48.1, and 50.2 can be readily attributed to the (202), (311), (222), (400), (440), and (531) crystalline plane of SIS, respectively. The results indicated that the presence of GO had little effect on the crystal structure of SIS. Furthermore, the grain size was also computed using the Scherrer relation [41,42]:

$$\text{Grain size} = 0.9 \times \lambda/\beta \cos\theta,$$

where λ represents the wavelength of the incident X-ray, θ represents the diffraction angle, and β represents the FWHM value for a given spike. The average crystallite sizes of the samples were estimated from the diffraction peak (440) to be 16.1, 13.8, 13.7, and 14.6 nm.

FT-IR spectrum was performed to further attest the existence of rGO in the rGO/SIS nanocomposites. As shown in Figure 6, three distinct characteristic peaks of GO at 1,045, 1,624, and 1,731 cm^{-1} can be assigned to C–OH, C═C, and C═O stretches, respectively. Compared with GO, FT-IR spectrum of rGO/SIS-2 nanocomposites exhibited the reduced intensity at 1,624 cm^{-1} and the two characteristic peaks located at 1,731 and 1,045 cm^{-1} vanished. All inferred that GO was reduced to rGO in the process of preparing rGO/SIS nanocomposites.

3.3 Optical performance

It is well-known that UV–vis DRS is an extremely important technique to characterize the optical performance of photocatalysts. As revealed in Figure 7a, rGO/SIS nanocomposites show evidently enhanced visible light absorption capability with increasing the initial weight ratio of GO, which can be on account of rGO with an excellent visible light absorption characteristics. Interestingly, with the increase in the amount of rGO, the absorption band edge moves gradually to a higher wavelength, indicating the band gap narrowing of rGO/SIS photocatalysts. To further prove this result, the band gap of SIS, rGO/SIS-1, rGO/SIS-2, and rGO/SIS-3 can be calculated according to the corresponding Tauc plots method [43]:

$$(\alpha h\upsilon)^{1/n} = B(h\upsilon - E_g),$$

where α, $h\upsilon$, B, and E_g represent the absorption coefficient, the photon's energy, the constant factor, and the optical band gap, respectively. Generally, n is related to the properties of semiconductors (n = 2 for indirect and n = 1/2 for direct transitions). The plot of $(\alpha h\upsilon)^2$ verses $h\upsilon$ based on the direct transition is shown in Figure 7b. Band gap values for semiconductors were evaluated by extension of the linear portion of the arches to the energy axis. The band gap values of SIS, rGO/SIS-1, rGO/SIS-2, and rGO/SIS-3 are 2.29, 2.24, 2.21, and 2.17 eV, respectively. The decrease in band

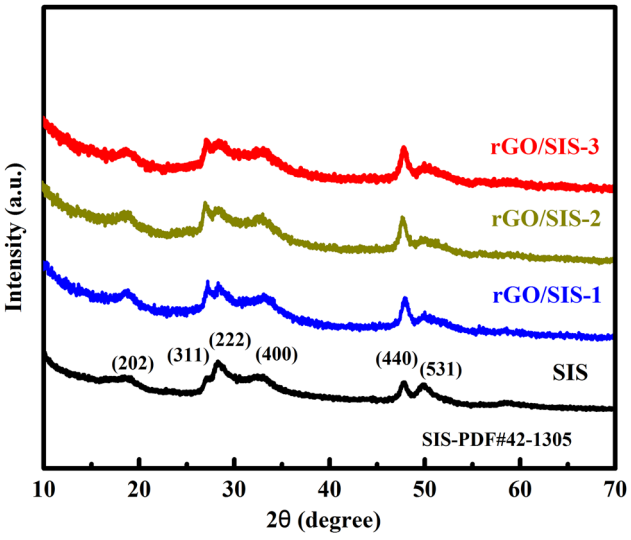

Figure 5: XRD patterns of SIS, rGO/SIS-1, rGO/SIS-2, and rGO/SIS-3.

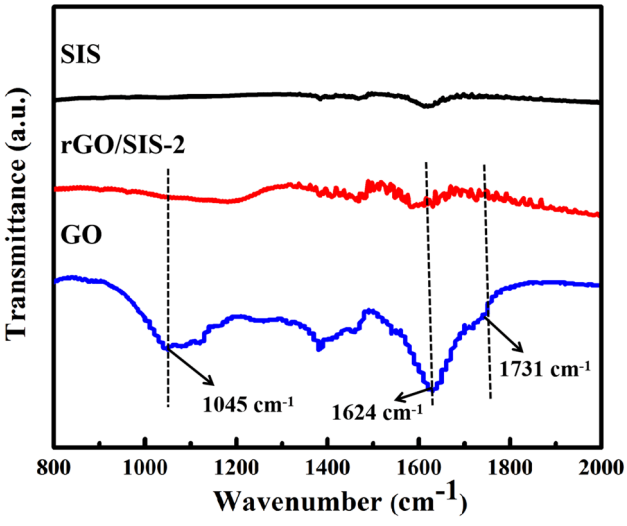

Figure 6: FT-IR spectra of SIS, rGO/SIS-2 and GO.

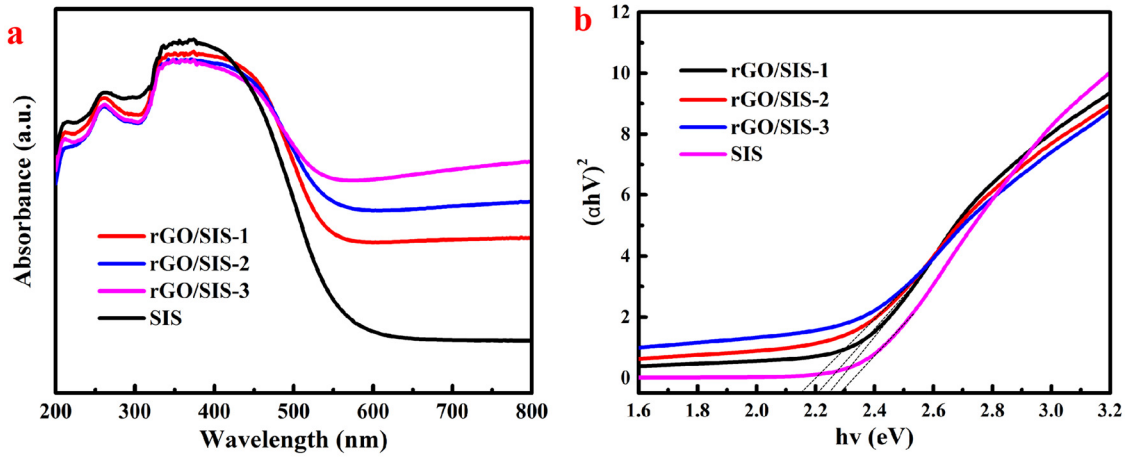

Figure 7: UV–vis DRS (a) and the corresponding $(\alpha h\upsilon)^2$ *versus* $h\upsilon$ curves (b) of SIS, rGO/SIS-1, rGO/SIS-2, and rGO/SIS-3.

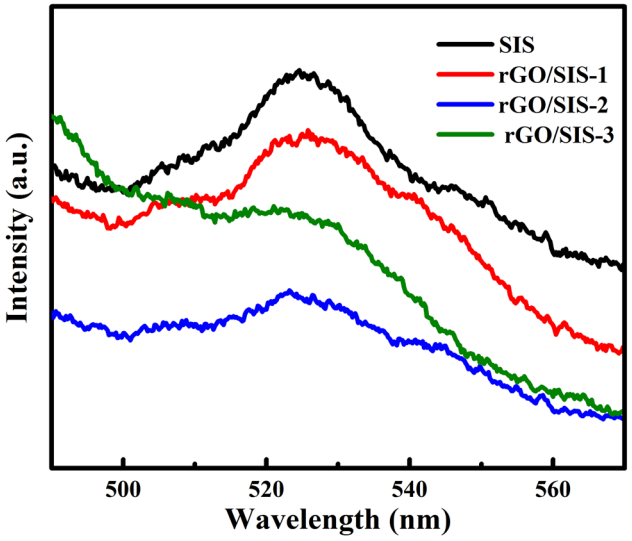

Figure 8: PL of SIS, rGO/SIS-1, rGO/SIS-2, and rGO/SIS-3.

gap may be aggregated to the intense interaction between SIS and rGO and excellent visible light absorption of GO. Meanwhile, the narrowed band gap of photocatalysts is ensured to be helpful for the transition and separation of photogenic electrons.

Photoluminescence spectra were used to further explore the separation efficiency of photogenic charge carriers. According to the principle of optoelectronics [44], when semiconductors are excited at a fixed wavelength and operating voltage, a large amount of the photogenerated electrons–holes will quickly recombine, generating fluorescence emission. In common, the lower fluorescence emission intensity represents higher separation efficiency of the photogenerated electrons–holes. In other words, the potocatalyst's weaker PL intensity implies that electron–hole pairs recombine at a slower pace [45], which was beneficial for improving the photocatalytic performance. As demonstrated in Figure 8, with the increasing amount of rGO, the fluorescence intensity gradually decreased, manifesting the separation efficiency of photogenerated electron–hole was obviously enhanced. Surprisingly, as rGO continued to be added, the fluorescence intensity tends to increase, which suggested that excess rGO could accelerate the recombination of photogenerated electron–hole pairs, causing the reduction of photocatalytic activity.

3.4 Photocatalytic activities of rGO/SIS nanocomposites

The photocatalytic activities of a series of rGO/SIS nanocomposites were executed with RhB as the target pollutant under visible light irradiation. As exhibited in Figure 9(a and b), rGO/SIS-1 and rGO/SIS-2 photocatalysts show enhanced photocatalytic activities toward the degradation of RhB in comparison with pure SIS. While for rGO/SIS-3, excessive rGO loading brings the decline in the photocatalytic efficiency. This is because an appropriate amount of rGO is conducive to the generation and transmission of photogenerated electrons at photocatalyst interfaces, while excessive rGO loading will block light penetration and promote electron–hole recombination. In addition, excessive GO leads to the aggregation of photocatalysts (Figure 1d), reducing catalytic efficiency. For the sake of further analyzing the process of the degradation of RhB, Figure 9a (inset) demonstrates the absorbance variations of RhB with rGO/SIS-2 photocatalysts at different visible light radiation times. It was found that the maximum absorption wavelength of residual RhB solution

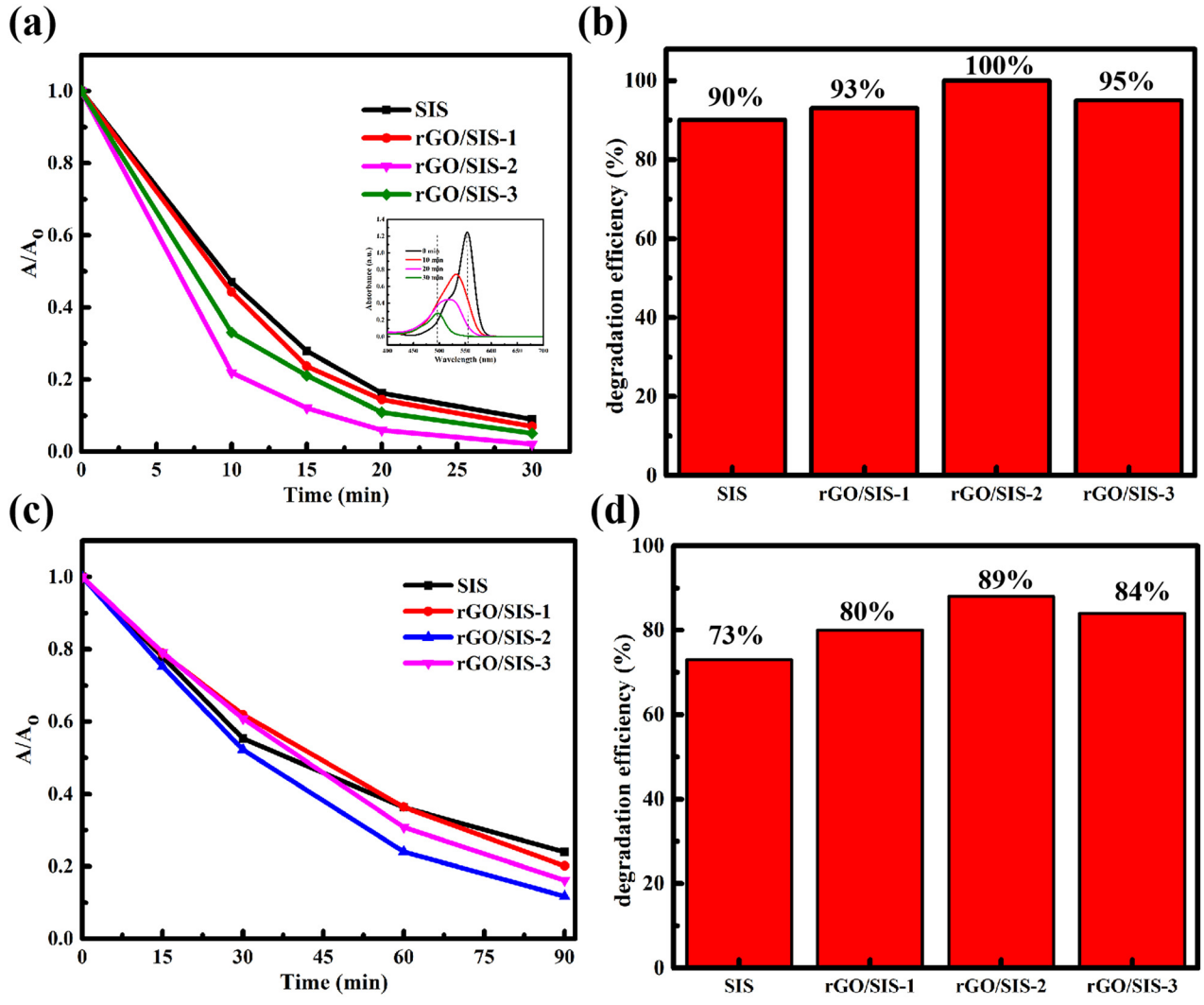

Figure 9: (a) Kinetics for decolorization of RhB (20 mg/L, 50 mL) and (b) DE of RhB with SIS, rGO/SIS-1, rGO/SIS-2, and rGO/SIS-3 photocatalysts; (c) kinetics for decolorization of MB (20 mg/L, 50 mL) and (d) DE of MB with SIS, rGO/SIS-1, rGO/SIS-2, and rGO/SIS-3 photocatalysts.

was transferred gradually from 554 to 499 nm, and RhB was completely degraded in 30 min in the presence of rGO/SIS-2 photocatalyst. Correspondingly, the color of the residual solution was gradually changed colorless. Furthermore, MB is also used as the other simulated dye pollutant. The absorbance spectra of the MB solution were also observed by using a UV–vis spectrophotometer at defined time intervals by comparing it with maximum band absorption at wavelength 664 nm. As shown in Figure 9(c and d), it can be seen that degradation ratios of MB in the presence of SIS, rGO/SIS-1, rGO/SIS-2, and rGO/SIS-3 photocatalysts can reach up to 73, 80, 89, and 84% after 90 min under the visible light irradiation, respectively, and rGO/SIS-2 shows the highest degradation rate. To highlight the significance of the present work, the photocatalytic activity of rGO/SIS-2 was compared to that of some other reported photocatalysts for the degradation of RhB (Table 1).

To further elucidate the process of photocatalysis, the mineralization efficiency of RhB was measured by a TOC analyser. As illustrated in Figure 10, with the extension of visible light irradiation time, the TOC removal efficiency of RhB increased, and finally reached up to 73.8% at 30 min, which was consistent with the result of the DE of RhB.

3.5 Recycle stability of photocatalysts

As a photocatalyst, the recycle stability is a key parameter to evaluate photocatalytic performance and is closely related to the practical application of photocatalysts. Herein, the catalytic characteristics of rGO/SIS-2 nanocomposites were investigated *via* three consecutive recycling experiments under the same conditions. After every cyclic experiment,

Table 1: Comparison of photocatalytic activity of rGO/SIS photocatalyst with some other reported photocatalysts for the degradation of RhB

Catalyst	Catalyst dose (mg)	Dye concentration (mg/L)	Dye volume (mL)	Degradation efficiency (%)	Degradation time (min)	Ref.
La-$CuFe_2O_4$/g-C_3N_4	60	30	150	97.35	48	[45]
WO_3/rGO/$SnIn_4S_8$	10	30	100	99	60	[46]
Mn-doped CuO	5	10	200	93.8	90	[47]
ZnO/CdO/CeO_2	10	10	50	73.16	70	[48]
Zn-doped CuO	5	15	75	92.89	70	[49]
Co/Fe-MOF	5	14.4	100	92	120	[50]
rGO/SIS	10	20	50	100	30	In this work

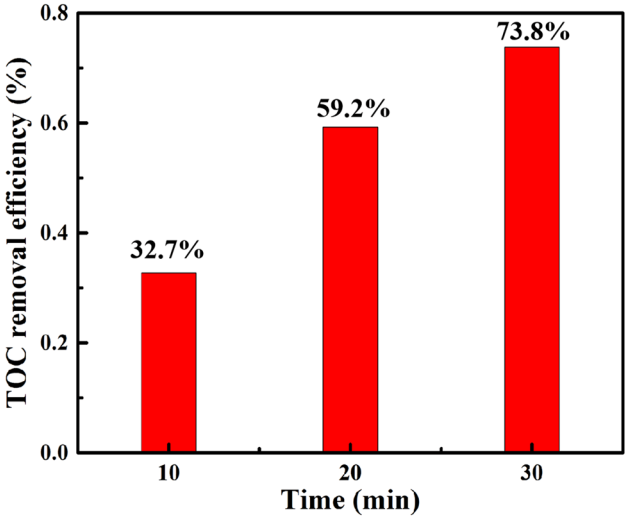

Figure 10: TOC removal efficiency of RhB on rGO/SIS photocatalysts under visible light irradiation.

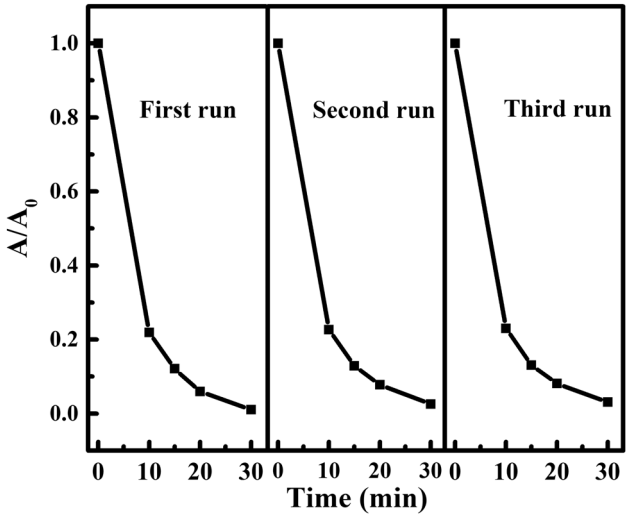

Figure 11: Recycle stability of rGO/SIS-2 photocatalysts on the photocatalytic removal of RhB with three recycling experiments in the RhB solution (20 mg/L, 50 mL) under visible light irradiation.

the samples were collected by centrifuge and washed with water and ethanol, respectively, and then used for the next experiment. The results revealed that the removal efficiency of RhB still remained 96% after three cycles (Figure 11), showing prominent recycle stability.

3.6 Photocatalytic mechanism

On the basis of the above-mentioned analyses, the conceivable mechanism for photocatalytic RhB degradation in the presence of rGO/SIS nanocomposites is exhibited in

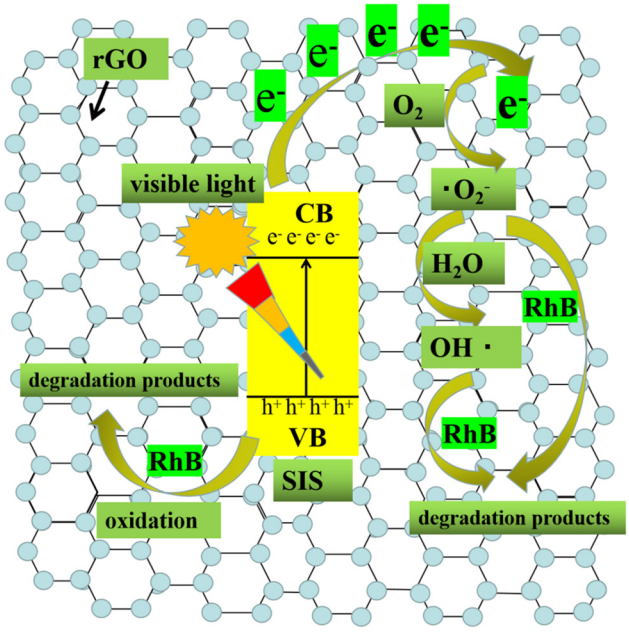

Figure 12: The proposed mechanism diagram for photocatalytic RhB degradation in the presence of rGO/SIS photocatalysts.

Figure 12. Under visible light irradiation, SIS photocatalysts are excited and generated photoinduced electrons (e^-) and holes (h^+) in their conduction band (CB) and valence band (VB), respectively. Afterwards, photoinduced electrons in the CB of SIS can be migrated into rGO, hindering the recombination of photoinduced electron and hole pairs. The photoinduced electrons in rGO could react with dissolved O_2 to produce $\cdot O_2^-$ radicals. Then, a good deal of $\cdot O_2^-$ radicals could quickly oxidize RhB to form degradation products. Furthermore, others can react with H_2O to generate $\cdot OH$, which can further interact with RhB to make degradation products. In the opposite direction, holes in the VB of SIS can directly oxidize RhB to generate degradation products. Therefore, on account of the strong interaction of rGO and SIS and enhanced utilization of visible light, the band gap energy of rGO/SIS photocatalysts is narrowed. Moreover, because of the high conductivity of graphene, the photoinduced electrons can migrate rapidly from CB of SIS to rGO, which would restrain the recombination of e^-–h^+ pairs, resulting in the improvement of photocatalytic performance. Furthermore, owing to excellent electrons' mobility of graphene, charge separation efficiency can be improved, which is also beneficial for enhancing photocatalytic activity.

4 Conclusion

In summary, a series of rGO/SIS nanocomposites were successfully fabricated *via* the microwave-assisted method. The results indicated that as the amount of rGO increased, the unchin-like microsphere structure of rGO/SIS evolved gradually into aggregated nanosheet structure. Moreover, appropriate amounts of rGO can decrease the band gap and accelerate the separation of photogenerated electron–hole. Importantly, the as-prepared nanocomposites were employed to degrade RhB under visible light illumination. In comparison with pure SIS with a 90% degradation rate, the optimal rGO/SIS-2 nanocomposites displayed enhanced photocatalytic activity with complete degradation to RhB within 30 min. Interestingly, rGO/SIS-2 nanocomposites exhibited excellent recycle stability with 96% removal efficiency of RhB after three cycles. Thus, the introduction of appropriate amounts of rGO can not only change the morphology of SIS but also enhance the visible light absorption, decrease band gap energy, and accelerate the separation and migration of photoinduced electron–hole. These results can be beneficial to enhance the photocatalytic efficiency of rGO/SIS nanocomposites. This work provides a facile and efficient pathway to prepare SIS-based nanocomposites by incorporating carbon-based nanomaterials for the degradation of organic pollutants in visible light irradiation.

Funding information: The authors would like to thank the financial support for this work from the Opening Project of the Key Laboratory of Leather Chemistry and Engineering (Sichuan University), Ministry of Education and the Synthetic Leather and High-Performance Fibers Innovation Team (2020SCUNG122).

Author contributions: All authors have accepted responsibility for the entire content of this manuscript and approved its submission.

Conflict of interest: The authors state no conflict of interest.

References

[1] Islam T, Repon MR, Islam T, Sarwar Z, Rahman MM. Impact of textile dyes on health and ecosystem: a review of structure, causes, and potential solutions. Environ Sci Pollut R. 2023;30(4):9207–42.

[2] Berradi M, Hsissou R, Khudhair M, Assouag M, Cherkaoui O, El Bachiri A, et al. Textile finishing dyes and their impact on aquatic environs. Heliyon. 2019;5(11):e0271.

[3] Alharthi FA, Albaeejan MA, Alshayiqi AA, Aldubeikl HK, Hasan I. Enhanced visible-light-driven photocatalytic degradation of azo dyes by heteroatom-doped nickel tungstate nanoparticles. Nanotechnol Rev. 2023;12(1):20230143.

[4] Khurana I, Saxena A, Bharti, Khurana JM, Rai PK. Removal of dyes using graphene-based composites: A review. Water Air Soil Pollut. 2017;228(5):180.

[5] Nasar A, Mashkoor F. Application of polyaniline-based adsorbents for dye removal from water and wastewater-a review. Environ Sci Pollut Res. 2019;26(6):5333–56.
[6] Li LW, Chi L, Zhang HX, Wu SM, Wang H, Luo ZM, et al. Fabrication of Ti-PDA nanoparticles with enhanced absorption and photocatalytic activities for hexavalent chromium Cr(VI) removal. Appl Surf Sci. 2022;580:152168.
[7] Jiao W, Shen W, Rahman ZU, Wang D. Recent progress in red semiconductor photocatalysts for solar energy conversion and utilization. Nanotechnol Rev. 2016;5(1):135–45.
[8] Geldasa FT, Kebede MA, Shura MW, Hone FG. Experimental and computational study of metal oxide nanoparticles for the photocatalytic degradation of organic pollutants: a review. RSC Adv. 2023;13(27):18404–42.
[9] Low J, Jiang C, Cheng B, Wageh S, Al-Ghamdi AA, Yu J. A review of direct Z-scheme photocatalysts. Small Methods. 2017;1(5):1–21.
[10] Ye MY, Pan JH, Guo Z, Liu XY, Chen Y. Effect of ball milling process on the photocatalytic performance of CdS/TiO_2 composite. Nanotechnol Rev. 2020;9(1):558–67.
[11] Wang J, Feng J, Wei C. Molecularly imprinted polyaniline immobilized on Fe_3O_4/ZnO composite for selective degradation of amoxycillin under visible light irradiation. Appl Surf Sci. 2023;609:155324.
[12] Jonathan R, Ur Rehman S, Cao F, Xu H, Ma XJ, Wang JW, et al. Low-cost and large-scale preparation of ultrafine TiO_2@C hybrids for high-performance degradation of methyl orange and formaldehyde under visible light. Nanotechnol Rev. 2023;12(1):20220556.
[13] Moghanlou AO, Sadr MH, Bezaatpour A, Salimi F, Yosefi M. RGO/Cu_2O-CuO nanocomposite as a visible-light assisted photocatalyst for reduction of organic nitro groups to amines. Mol Catal. 2021;516:111997.
[14] Yu HG, Chu CL, Chu PK. Self-assembly and enhanced visible-light-driven photocatalytic activity of reduced graphene oxide-Bi_2WO_6 photocatalysts. Nanotechnol Rev. 2017;6(6):505–16.
[15] Han C, Cheng C, Liu FL, Li XL, Wang GX, Li JW. Preparation of CdS-Ag_2S nanocomposites by ultrasound-assisted UV photolysis treatment and its visible light photocatalysis activity. Nanotechnol Rev. 2023;12(1):20220503.
[16] Munonde TS, Nomngongo PN. Review on metal chalcogenides and metal chalcogenide-based nanocomposites in photocatalytic applications. Chem Afr. 2023;6(3):1127–43.
[17] Oluwalana AE, Ajibade PA. Preparation and morphological studies of tin sulfide nanoparticles and use as efficient photocatalysts for the degradation of rhodamine B and phenol. Nanotechnol Rev. 2022;11(1):883–96.
[18] Chen A, Zhang J, Zhou Y, Tang H. Preparation of a zinc-based metal–organic framework (MOF-5)/BiOBr heterojunction for photodegradation of Rhodamine B. React Kinet Mech Catal. 2021;134(2):1003–15.
[19] Kumary A, Pillai NG, Rhee KY, Park S, Azeez AA. Encapsulation strategies for improving the biological behavior of CdS@ZIF-8 nanocomposites. Nanotechnol Rev. 2022;11(1):2661–72.
[20] Chen CC, Shaya J, Polychronopoulou K, Golovko VB, Tesana S, Wang SY, et al. Photocatalytic degradation of ethiofencarb by a visible light-driven $SnIn_4S_8$ photocatalyst. Nanomaterials. 2021;11(5):1–17.
[21] Lan M, Jia H, Dong X, Zheng N, Li X, Wang Y, et al. Design and construction of $SnIn_4S_8$/$Cd_{0.5}Zn_{0.5}S$ heterostructurephotocatalyst for efficient Cr(VI) reduction. Mol Catal. 2023;551:113622.
[22] Deng F, Pei X, Luo Y, Luo X, Dionysiou DD, Wu S, et al. Fabrication of hierarchically porous reduced graphene oxide/$SnIn_4S_8$ composites by a low-temperature co-precipitation strategy and their excellent visible-light photocatalytic mineralization performance. Catalysts. 2016;6(8):113.
[23] Shi H, Wang C, Zhao Y, Liu E, Fan J, Ji Z. Highly efficient visible light driven photocatalytic inactivation of E. coli with Ag QDs decorated Z-scheme Bi_2S_3/$SnIn_4S_8$ composite. Appl Catal B Environ. 2019;254:403–13.
[24] Lu M, Wang X, Zhang Y, Li Z, Xu S, Yao C. Facile synthesis of a symmetrical squarylium dye sensitized $SnIn_4S_8$ composites with enhanced photocatalytic activity under visible-light irradiation. J Mater Sci Mater Electron. 2017;28(21):15987–95.
[25] Deng F, Lu X, Zhao L, Luo Y, Pei X, Luo X, et al. Facile low-temperature co-precipitation method to synthesize hierarchical network-like g-C_3N_4/$SnIn_4S_8$ with superior photocatalytic performance. J Mater Sci. 2016;51(14):6998–7007.
[26] Tang C, Xiong R, Li K, Xiao Y, Cheng B, Lei S. Spatially distributed Z-scheme heterojunction of g-C_3N_4/$SnIn_4S_8$ for enhanced photocatalytic hydrogen production and pollutant degradation. Appl Surf Sci. 2022;598:153870.
[27] Shen CH, Chen Y, Xu XJ, Li XY, Wen XJ, Liu ZT, et al. Efficient photocatalytic H_2 evolution and Cr(VI) reduction under visible light using a novel Z-scheme $SnIn_4S_8$/CeO_2 heterojunction photocatalysts. J Hazard Mater. 2021;416:126217.
[28] Sun M, Li F, Su M, Wei D, Yang Q, Yan T, et al. Fabrication of MOF-derived tubular In_2O_3@$SnIn_4S_8$ hybrid: Heterojunction formation and promoted photocatalytic reduction of Cr(VI) under visible light. J Colloid Interface Sci. 2021;596:278–87.
[29] Hu M, Yan A, Huang J, Huang F, Li F, Cui Q, et al. Novel 2D hybrids composed of $SnIn_4S_8$nanoplates on BiOBr nanosheets forenhanced photocatalytic applications. Nanotechnology. 2020;31:105202.
[30] Rahimi K, Zafarkish H, Yazdani A. Reduced graphene oxide can activate the sunlight-induced photocatalytic effect of NiO nanowires. Mater Des. 2018;144:214–21.
[31] Liu B, Lin L, Yu D, Sun J, Zhu Z, Gao P, et al. Construction of fiber-based $BiVO_4$/SiO_2/reduced graphene oxide (RGO) with efficient visible light photocatalytic activity. Cellulose. 2018;25(2):1089–101.
[32] Mathew J, John N, Mathew B. Graphene oxide-incorporated silver-based photocatalysts for enhanced degradation of organic toxins: a review. Environ Sci Pollut R. 2023;30:16817–51.
[33] Xu P, Huang S, Lv Y, Chen Y, Liu M, Fan H. Surfactant-assisted hydrothermal synthesis of rGO/$SnIn_4S_8$ nanosheets and their application in complete removal of Cr(VI). RSC Adv. 2018;8(11):5749–59.
[34] Cheng C, Shi Q, Zhu W, Zhang Y, Su W, Lu Z, et al. Microwave-assisted synthesis of MoS_2/$BiVO_4$ heterojunction for photocatalytic degradation of tetracycline hydrochloride. Nanomaterials. 2023;13(9):1522.
[35] Naik MM, Yashwanth HJ, Vinuth M, Nagaraju G, Hareesh K, Naik HSB. Microwave radiation assisted synthesis of $NiFe_2O_4$-$CoFe_2O_4$ nanocomposites for photocatalytic and photoelectrochemical water splitting applications. Inorg Chem Commun. 2024;160:111898.
[36] Zhang M, Wang M, Liu X, Huang H, Zhao S, Ma J, et al. Microwave-hydrothermal synthesis of F and Fe co-doped CeO_2 photocatalysts for efficient removal of 2,4,6-TCP under visible light. Mater Sci Semicond Process. 2024;171:108032.
[37] Song R, Chen N, Han B, Yu S, Wang Y, Liu K, et al. Microwave hydrothermal fabrication of 3D hierarchical Br/Bi_2WO_6 with enhanced photocatalytic activity for Rhodamine B and tetracycline degradation. Environ Sci Pollut R. 2021;28:36434–52.
[38] Lai S, Jin Y, Shi L, Zhou R, Li Y. Fluorescence sensing mechanisms of versatile graphene quantum dots toward commonly encountered heavy metal ions. ACS Sens. 2023;8(10):3812–23.

[39] Aamir M, Bibi I, Sabir M, Mubarik S, Raza Q, Karami A, et al. Binary metal doped and graphene anchored $LaCrO_3$ perovskite with boost light harvesting properties for environmental remediation. Opt Mater. 2023;145:114390.
[40] Wang Z, Zhao J, Gao Q, Luo H, Fan H, Xiang J, et al. Urchin-like $SnIn_4S_8$ photocatalyst synthesized via microwave assisted method with durable photocatalytic performance under visible light. Chem Phys Lett. 2023;817:140409.
[41] Wazir W, Ahmad Z, Zulfiqar S, Cochran E, Mubarik S, Kousar T, et al. Synergistic effects of noble metal doping and nanoengineering on boosting the azo dye mineralization activity of nickel oxide. Ceram Int. 2023;49:38026–35.
[42] Li T, Aadil M, Zulfiqar S, Anwar A, Yakout S, Panduro-Tenazoa N, et al. Synthesis of doped and porous CuO with boosted light-harvesting features for the photocatalytic mineralization of azo dyes. Ceram Int. 2023;49:27827–36.
[43] Alshammari R, Aadil M, Kousar T, Maqbool U, Ahmad Z, Alswieleh A, et al. Synthesis of binary metal doped CuO nanoarchitecture for congo red dye removal: Synergistic effects of adsorption and mineralization techniques. Opt Mater. 2023;144:114314.
[44] Raja A, Son N, Pandey S, Kang M. Fabrication of solar-driven hierarchical $ZnIn_2S_4$/rGO/SnS_2 heterojunction photocatalyst for hydrogen generation and environmental pollutant elimination. Sep Purif Technol. 2022;293:121119.
[45] Ahmed A, Alabada R, Usman M, Alothman A, Tufail M, Mohammad S, et al. Synthesis of visible-light-responsive lanthanum-doped copper ferrite/graphitic carbon nitride composites for the photocatalytic degradation of toxic organic pollutants. Diam Relat Mater. 2024;141:110630.
[46] Xu P, Huang S, Liu M, Lv Y, Wang Z, Long J, et al. Z-schemed WO_3/rGO/$SnIn_4S_8$ sandwich nanohybrids for efficient visible light photocatalytic water purification. Catalysts. 2019;9(2):187.
[47] Tamam N, Aadil M, Hassan W, Ejaz S, Najm Z, Alsafari I, et al. Surfactant assisted synthesis of nanostructured Mn-doped CuO: An efficient photocatalyst for environmental remediation. Ceram Int. 2022;48(20):29589–600.
[48] Ishfaq M, Hassan W, Sabir M, Somaily H, Hachim S, Kadhim Z, et al. Wet-chemical synthesis of ZnO/CdO/CeO_2 heterostructure: A novelmaterial for environmental remediation application. Ceram Int. 2022;48(23):34590–601.
[49] Aadil M, Hassan W, Somaily H, Ejaz S, Abass R, Jasem H, et al. Synergistic effect of doping and nanotechnology to fabricate highly efficient photocatalyst for environmental remediation. J Alloy Compd. 2022;920:165876.
[50] Tran T, Ho H, Nguyen H, Tran B, Nguyen T, Bui P, et al. Photocatalytic degradation of Rhodamine B in aqueous phase by bimetallic metal-organic framework M/Fe-MOF (M = Co, Cu, and Mg). Open Chem. 2022;20(1):52–60.